Theoretical Modeling and Design Guidelines for a New Class of Wearable Bio-Matched Antennas

John Blauert, *Student Member, IEEE*, and Asimina Kiourti, *Senior Member, IEEE*

***Abstract*— We present theoretical modeling and design guidelines for Bio-Matched Antennas (BMAs), an emerging class of wearable, into-body antennas that surpass the state-of-the-art in terms of bandwidth and gain. In brief, BMAs are ultra-wideband, pyramid-shaped antennas that utilize the periodic combination of water and plastic to enhance performance. The new modeling enables customized performance for applications as diverse as radiometry, telemetry with implants, and more. Our studies utilize a comparison of the BMA to a conical antenna to model the low frequency cutoff. In addition, we conduct a Plane Wave Expansion Method analysis of the engineered periodic dielectrics to: a) model the high frequency cutoff of the BMA, and b) to predict the permittivity of the Bio-Matched dielectric. Parametric studies are further pursued to assess transmission loss as a function of the BMA's height. We verify our design framework through a novel BMA that operates from 1-12 GHz with 21.4 dB of transmission loss through 3 cm of tissue at 2.4 GHz. Compared to the most wideband and most efficient into-body radiator previously reported, this is 6.2 dB less transmission loss, with the new design also exhibiting nearly twice as much bandwidth.**

***Index Terms*— Biomedical telemetry, engineered dielectrics, into-body antenna, wearable antenna.**

I. Introduction

RADIO frequency (RF) devices, including wearables and implants, play a key role in emerging medical technologies. Many of these devices, such as radiometers and wireless implants, rely on into-body radiation. Specifically, medical radiometry is a non-invasive imaging/sensing technology that allows for improved detection of core body temperature [1]-[3] and cancer [4] through monitoring RF radiation from the body. As another example of into-body radiators, implanted medical devices, such as neural implants [5], pacemakers [6], and glucometers/insulin pumps [7]-[8], can be made more ubiquitous through efficient wireless links with into-body radiators. In turn, extensive research has been conducted into efficient implanted antennas that can communicate from within the body to outside of it for implant telemetry [9]-[17] and/or wireless charging [18]. Indeed, numerous papers have demonstrated that it is possible to have reliable and optimally efficient data links within microwave frequencies to such devices [19]-[22]. As expected, the aforementioned medical technologies necessitate robust, wideband and high gain wearable antennas to act as into-body radiators. Such features will eventually allow for high sensitivity radiometers and high data-rate telemetry links for implants.

To date, very few works have reported on into-body radiators for radiometry applications, and most of them do not address transmission loss aspects, Table I [1]-[4]. Instead, radiometry research focuses primarily on antenna bandwidth and backend signal processing to interpret the received thermal radiation. In contrast, works on into-body radiators intended for telemetry with implants often provide data link efficiency for benchmarking performance. Table II provides an overview of such state-of-the-art into-body antennas and their associated performance [9]-[17]. While a variety of phantom setups and thicknesses are used, our antenna still shows a marked improvement compared to the state of the art.

As seen in Table II, several implant communication systems utilize off-body radiators, i.e., radiators that are separated from the patient by a sizeable air gap [9]-[13]. However, the immense mismatch between biological tissues and free space adds an additional insertion loss. Indeed, air-tissue mismatch loss for a cardiac model wireless link operating at 2.4 GHz has been found to be as high as 17.5 dB [12]. To mitigate this mismatch loss, research has been conducted on wearable, into-body antennas that make direct contact with the body [14]-[17]. Most designs are relatively two-dimensional, utilizing a modified patch antenna milled from printed circuit board laminates. However, such antennas still have numerous issues to overcome: (a) mismatch at the biological tissue and antenna interface, (b) environmental and inter-subject variability, (c) frequency-dependent tissue properties, and (d) inherent material loss of biological tissues [17].

To address these concerns, we recently reported a prototype antenna that utilizes an engineered periodic dielectric composed

Manuscript received May 22nd, 2019, revised October 1st, 2019.
J. Blauert and A. Kiourti are with the ElectroScience Laboratory, Dept. of Electrical and Computer Engineering, The Ohio State University, Columbus, OH, USA (e-mail: blauert.1@osu.edu, kiourti.1@osu.edu).

This is the author's version of an article that has been published in this journal. Changes were made to this version by the publisher prior to publication.
The final version of record is available at http://dx.doi.org/10.1109/TAP.2019.2948727

TABLE I. INTO-BODY RADIATORS FOR RADIOMETRY: COMPARISON OF PROPOSED DESIGN VS. THE STATE OF THE ART

Ref.	Size / Antenna Type	Phantom Used	Bandwidth
[1]	$\pi \times 12.5^2 \times 4.45$ mm^3 / Spiral	Chemical phantoms to represent brain	1.1-1.6 GHz
[2]	$40 \times 10 \times 5$ mm^3/ Biconical Patch	Simulation of breast tissue	1-4 GHz
[3]	$40 \times 40 \times 2.54$ mm^3 / Patch	Salmon/water to represent skin/muscle	1.4-1.427 GHz
[4]	$21 \times 27 \times \sim 30$ mm^3 / Waveguide	Chemical phantoms to represent brain	1-4 GHz
This work	$24.9 \times 24.9 \times 11.95$ mm^3 / Horn	Beef/POPEYE	1.07-11.9 GHz

TABLE II. INTO-BODY RADIATORS FOR TELEMETRY: COMPARISON OF PROPOSED DESIGN VS. THE STATE OF THE ART

Ref.	Frequency	Implantation Depth	Air Gap	Size / Antenna Type	Bandwidth	Transmission Loss
[9]	2.4 GHz	3.3 mm	4 mm	$\pi \times 72.5^2 \times 13.635$ mm^3 / Spiral	0.6-6 GHz	26 dB
	4.8 GHz	3.3 mm	4 mm	$\pi \times 72.5^2 \times 13.635$ mm^3 / Spiral	0.6-6 GHz	19 dB
[10]	400 MHz	4 mm	5 cm	375 mm / Dipole	NA	34 dB
	2.4 GHz	4 mm	5 cm	62.4 mm / Dipole	NA	32 dB
[11]	2.4 GHz	3.5 cm	10 cm	NA / Free-Space Horn	0.9-2.45 GHz	56.5 dB
[12]	400 MHz	1 cm	1.5 cm	$70 \times 60 \times 1.6$ mm^3 / Patch	350-450 MHz	50 dB
[13]	2.4 GHz	5 cm	2.55 m	NA / Free-Space Horn	NA	81 dB
[14]	2.4 GHz	4 mm	0 cm	$26.3 \times 30 \times 1.6$ mm^3 / Spiral	2-11 GHz	22.5 dB
[15]	400 MHz	9 mm	0 cm	$28 \times 26.8 \times 0.635$ mm^3 / Patch	380-470 MHz	24 dB
[16]	2.4 GHz	2 cm	0 cm	$\pi \times 17.5^2 \times 0.76$ mm^3 / Exponentially Tapered Slot	2.35-2.7 GHz	30 dB
[17]	2.4 GHz	2 cm	0 cm	$22 \times 22 \times 10$ mm^3 / BMA	1.4-8.5 GHz	19.2 dB
This work	2.4 GHz	3 cm	0 cm	$24.9 \times 24.9 \times 11.95$ mm^3 / BMA	1.07-11.9 GHz	21.4 dB

of plastic and water to match to biological tissues over a wide bandwidth [17]. This antenna was referred to as the Bio-Matched Horn and was shown to operate from 1.4-8.5 GHz with 10.8 dB less transmission loss compared to the state-of-the-art at 2.4 GHz [17]. The high gain in combination with the remarkably wide bandwidth of this antenna allows for robust RF transmission through biological tissues. This is not the first inclusion of water in medical antenna design, as [23] utilized water inside of an ingestible antenna. However, [17] was the first to utilize the periodic inclusion of water with a low permittivity material for an effective bio-matched material.

Given the success of our proof-of-concept prototype, a comprehensive theoretical framework is developed and reported in this paper. Having such a framework scales the design from a single prototype to a full class of antennas. We refer to these antennas as Bio-Matched Antennas (BMAs): a new class of wearable, high-gain, wideband antennas that can be fine-tuned according to design guidelines introduced in this work to fit numerous into-body applications. It is worth clarifying here that the initial prototype of [17] was referred to as a Bio-Matched Horn based upon design shape and appearance. However, traditional metal-waveguide-excited horn antennas [24] operate differently than the BMAs, which are more closely related to a conical antenna [25]. In order to avoid confusion, the new class of antennas shall be referred to as BMAs.

While [17] demonstrated a unique approach to into-body radiator designs, there was little discussion of the theory behind this concept. The paper reported only a proof-of-concept design that was not optimized in any way. Understanding the fundamental governing equations behind the BMA's performance would allow for custom designs with optimized performance for various application scenarios. For example, larger BMAs can operate at lower frequencies but have higher loss at higher frequencies as compared to smaller BMAs. As another example, increasing the unit cell size allows for easier manufacturing and quicker simulation times but lowers the high frequency cutoff.

In this paper, we build on a parameterized BMA design and develop a thorough theoretical framework that allows for customizable designs. Simulation results are reported and further validated by measurements using tissue-emulating phantoms. To validate and demonstrate the utility of our design framework, we design, fabricate and measure a BMA with 6.2 dB less transmission loss and a 11.12:1 as opposed to a 6.07:1 bandwidth than [17] at a minimal increase in antenna

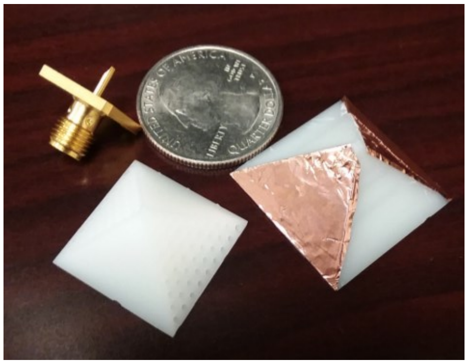

(a)

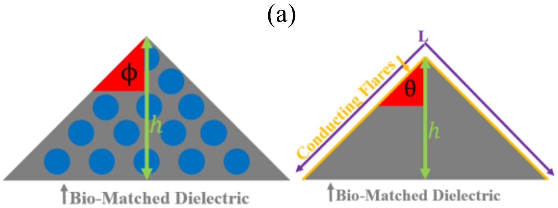

(b)

Fig. 1. (a) Prototype BMA with U.S. quarter for size comparison. (b) BMA cross-sections with parameters shown. Conducting flares (orange) coat a Bio-Matched dielectric (gray with blue).

dimensions. Comparison vs. the state of the art is shown in Tables I and II.

The rest of the paper is organized as follows. Section II presents the BMA model and design parameters. Section III discusses the theory behind engineering the Bio-Matched dielectric. Section IV reports design guidelines relating to the antenna performance, whereas Section V explores the model verification through measurement. The paper concludes in Section VI.

II. BMA Model and Design Parameters

A fabricated BMA is shown in Fig. 1(a) with indicative cross-section diagrams for BMAs shown in Fig. 1(b). The antenna consists of two conducting flares that surround a Bio-Matched dielectric on two opposite sides of ascending angles θ and ϕ. Unless specified otherwise, the ascent angle is uniform in both directions and is referred to solely as θ. The BMA can be excited via a Sub-Miniature Version A (SMA) connector being applied along the top of the antenna with the pin touching one flare and the ground plane touching the other flare. The pyramidal shape allows for the antenna to behave like a dielectrically loaded conical antenna, enabling wide bandwidth and high gain. The BMA height, h, governs how much the antenna extends from the body. The BMA edge length, L, is the maximum length that copper extends along the flare.

The Bio-Matched dielectric plays a central role in BMA design. As is well known, the electrical properties (permittivity and conductivity) of biological tissues are heavily influenced by their high water content [26]. With this in mind, the proposed dielectric is engineered to mimic the properties of biological tissues through a periodic distribution of water surrounded by plastic. The unit cell (fundamental repeating structure) can take on different forms as will be discussed in Section III.

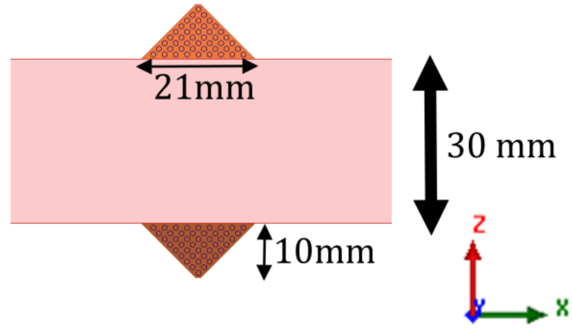

(a)

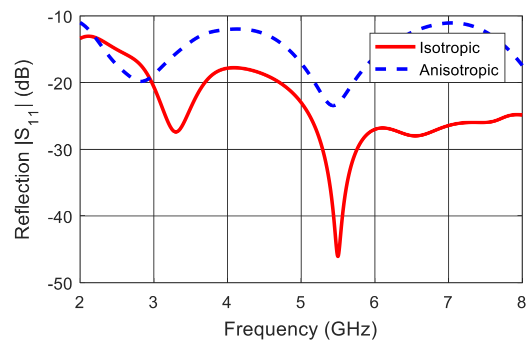

(b)

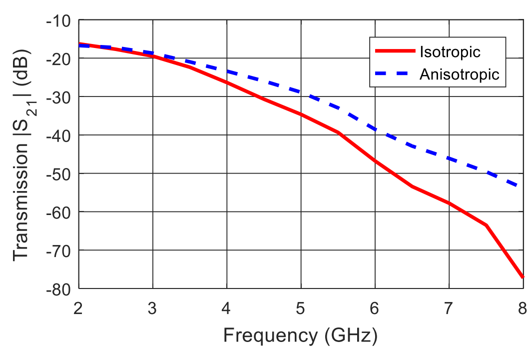

(c)

Fig. 2. Evaluating the benefitis of anisotropy: (a) simulation setup, (b) reflection coefficients for the BMAs, and (c) transmission loss between identical BMAs through 3 cm of tissue.

III. Engineering the Bio-Matched Dielectric

A. Benefits of Anisotropy

When engineering the dielectric to match to biological tissues, we have the freedom to design the dielectric to be isotropic or anisotropic. We posit that having a high permittivity in the plane orthogonal to propagation (xy-plane per Fig. 2(a)) and a low permittivity in the direction of propagation (z-direction per Fig. 2(a)) will improve the gain of the antenna. To test this hypothesis, we simulated two BMAs with lossless isotropic and anisotropic dielectrics, and compared their performance. For the isotropic case, the dielectric was defined to emulate the skin's permittivity in all directions. For the anisotropic case, the dielectric was composed of lossless versions of the materials used in [17] (water surrounded by PLA). Both BMAs have a height of 10 mm and θ=ϕ=45°.

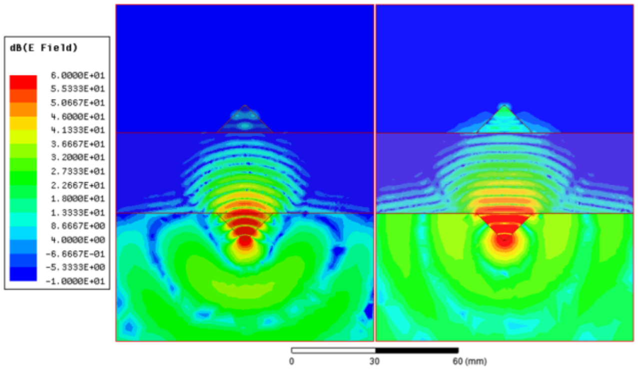

(a) (b)

Fig. 3. Electric fields at 8 GHz are more spherical for the (a) isotropic BMA and more planar for the (b) anisotropic BMA.

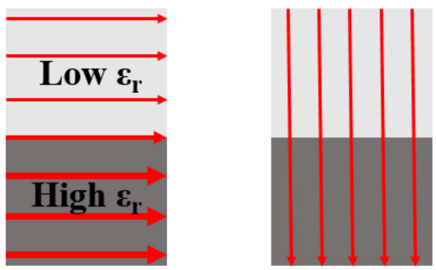

(a) (b)

Fig. 4. Electric flux developed: (a) strongly with parallel paths, and (b) weakly with orthogonal paths.

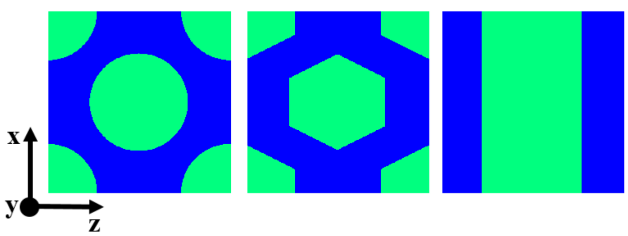

(a) (b) (c)

Fig. 5. Various unit cells can be designed, such as: (a) cylindrical, (b) hexagonal, and (c) rectangular. Here, different colors indicate materials of different permittivities (water in light green, plastic in dark blue).

Simulations were carried out in ANSYS High Frequency Structure Simulator (HFSS) using the setup of Fig. 2(a). As seen, two BMAs were employed, separated by a 30-mm-thick material emulating skin tissue. Skin tissue was chosen, because it is comparable in properties to ground beef and 2/3 muscle, both of which have been extensively used in the literature to emulate the average human body properties [9], [17], [27].

Simulated reflection coefficient results demonstrate that both BMAs are well matched, but the isotropic one is even better matched, as shown in Fig. 2(b). Simulated transmission coefficient results, shown in Fig. 2(c), indicate that the anisotropic permittivities achieve better transmission across the bandwidth. This is attributed to the orientation of the permittivities so that only the desired direction of propagation has a high permittivity path in the orthogonal plane. To better visualize how the anisotropic materials improve gain, the electric fields for the isotropic and anisotropic BMAs are shown in Figs. 3(a)-(b), respectively.

B. Development of Anisotropy

Since anisotropic materials are shown to perform better than isotropic, we must then consider how to develop anisotropy. One way to achieve anisotropy is through manipulating the orientation of materials of differing permittivity. In our case, these materials are selected to be plastic and water for reasons reported in Section II. Fig. 4 shows how the electric flux (red arrows) develops differently depending on direction, with dark grey representing a material with high permittivity (water) and light grey representing a material with low permittivity (plastic). Since the electric flux does not vary in the medium, an electric field applied to the medium will have a higher flux when having parallel paths of different dielectrics (shown in Fig. 3(a)) as opposed to being applied orthogonally through multiple media (shown in Fig. 3(b)). This principle is also the reason why series capacitors result in a lower capacitance than in a parallel arrangement [28]. Periodic distribution of a fundamental unit cell that has anisotropy due to such high and low flux paths will create an effective anisotropic medium. By controlling the ratio of high to low permittivity materials, the effective permittivity can be designed to match to a propagating medium.

C. Unit Cell Choice and Design

Referring to Fig. 5(a), the unit cell employed in [17] was a cylindrical water (in light green) unit cell surrounded by plastic (in dark blue). However, other unit cells can be designed, such as hexagonal and rectangular unit cells, shown in Fig. 5(b) and 5(c), respectively. The key merits of different unit cell designs lie in miniaturization and anisotropy. Miniaturization increases the high frequency cutoff and will be discussed further in Section IV-B, while anisotropy improves transmission as indicated previously in Section III-A.

In brief, hexagonal unit cells are superior to cylindrical unit cells in both miniaturization and anisotropy considerations [29]. Rectangular unit cells offer comparable anisotropy to cylindrical unit cells, but enable a much higher degree of miniaturization than both cylindrical and hexagonal designs. Here, it is worth nothing that all three unit cells of Fig. 5 are uniaxial in design, meaning they have one permittivity direction that is abnormal to the rest [28]. However, they differ in type of birefringence (degree of anisotropy) developed. Hexagonal and cylindrical unit cells have positive birefringence, since the high permittivity path is solely in the y-direction. In contrast, rectangular unit cells have negative birefringence, since both the x- and y-directions have high permittivity paths and the z-direction has a low permittivity path [28].

D. Analysis of the Anisotropic Behavior

The Plane Wave Expansion Method (PWEM) [30] is hereafter used to analyze the anisotropic behavior of the Bio-Matched dielectric. The method solves Maxwell's equations in Fourier space, and, since the material is periodic, separates its

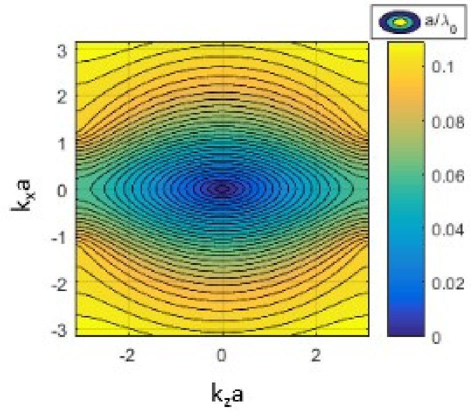

(a)

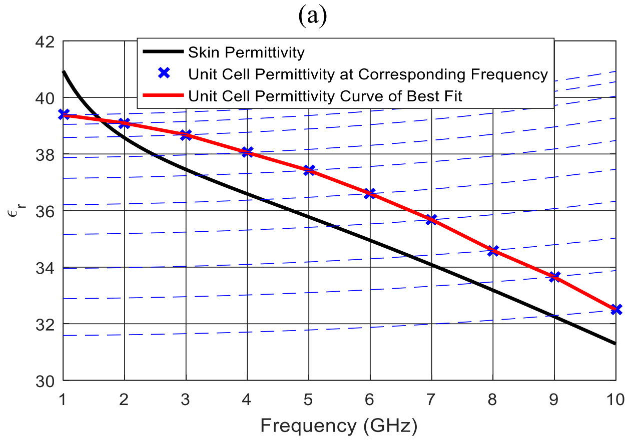

(b)

Fig. 6. PWEM used to develop: (a) isofrequency contour plots, and (b) effective permittivity vs. frequency plots.

operation across various frequencies into different bands. The first band can be considered as the effective medium band, and typically covers free-space wavelengths under ~0.05a, where "a" is the unit cell size. Depending on unit cell type, the first band cutoff can vary around this general estimate [30].

More specifically, the PWEM solves for the potential wave vectors for a given material structure. Here, this is done for the rectangular unit cell shown in Fig. 5(c), but can be readily expanded to other unit cells as well. One way to view the results of the PWEM is through the use of isofrequency contours as shown in Fig. 6(a). These contours are plotted for the unit cell size (a) divided by the free space wavelength (λ_0) for various wave vectors (k_x, k_z) scaled by the unit cell size (a).

As a next step, the effective permittivity of the medium can be extrapolated from the isofrequency contour plot, as shown by Fig. 6(b) [30]. Here, each of the dashed lines corresponds to the solved PWEM permittivity values in the x-direction at a given frequency. Notably, the PWEM is limited, because it only takes into account one frequency's electrical properties. Since water is highly dispersive, it needs to be implemented multiple times to account for the changing electrical properties with frequency. As such, each of these frequency-dependent curves will only remain valid at one point marked with a blue X. In turn, the effective permittivity needs to be solved at multiple points to develop a smooth curve over a wide bandwidth (see red line). For this example case, the maximum percentage difference between the skin and unit cell permittivities is smaller than 4.76% across the entire 1 to 10 GHz bandwidth plotted in Fig. 6(b).

IV. Modeling of the BMA Performance

This Section discusses how to modify BMA design aspects to customize antenna performance. Section IV.A discusses how unit cell size relates to the high frequency cutoff, whereas Section IV.B describes how the low frequency cutoff relates to antenna size. The real input impedance is described as relating to the flare angles and water concentration in Section IV.C, and the optimal transmission for a BMA is studied for various sizes in Section IV.D. All relations are hereafter studied through simulating BMAs that employ the rectangular unit cell of Fig. 5(c). This unit cell is chosen as attributed to: (a) the reduced simulation time, and (b) the fact that this unit cell can be easily manipulated with flare angle. In contrast, the hexagonal and cylindrical unit cells can only be implemented with a 45° flare angle, or else the edge of the BMA will cut through the water holes. To demonstrate how the developed framework can be generalized to other unit cells besides rectangular, a discussion is included in Section IV.E.

While a wide variety of tissue models may be considered in simulations depending on anatomical region, analysis in Section IV considers a homogeneous skin tissue model. This is because we intend to set a simple standard in place that can show the general trends for various applications. Skin tissue is chosen as it is the first layer of electromagnetic propagation and exhibits electrical properties close to those of 2/3 muscle (as often used to emulate the average human body properties) [26], [27].

In our simulations, we used the permittivity and loss tangent of water reported in [31]. The inclusion of water adds considerable loss to the antenna performance. However, the added benefits of broadband matching and antenna miniaturization outweigh the cost of loss. At microwave frequencies, there is minimal difference in loss tangent between distilled, deionized, and tap water [32]. This stems from the loss being primarily dielectric rather than conductive in nature.

A. High Frequency Cutoff

As seen in Fig. 6(b), the permittivity increases dramatically when the unit cell becomes electrically large (i.e., at high frequencies). This causes the unit cell to no longer behave like an effective medium, thus limiting the bandwidth of the BMA by restricting its upper frequency limit. To analytically derive the high frequency cutoff, parametric studies of the BMA are conducted in simulation.

For the rectangular unit cell of Fig. 5(c), a typical effective medium band extends from DC to wavelengths that are 0.05a (with "a" being the unit cell size) [30]. To study the exact cutoff, the rectangular unit cell BMA was simulated against skin and the high frequency cutoff was determined to be where the reflection coefficient is greater than -10 dB. Under these conditions, the free space cutoff wavelength (λ_0) can be modeled as being linearly related to the unit cell size (a) an offset based upon the water fill ratio (r), as shown in Eq. 1(a). The slope of this linear relationship, K, between the cutoff wavelength and unit cell size was parametrically studied in simulation as well. As shown in Eq. 1(b), K is increased by both

This is the author's version of an article that has been published in this journal. Changes were made to this version by the publisher prior to publication.
The final version of record is available at http://dx.doi.org/10.1109/TAP.2019.2948727

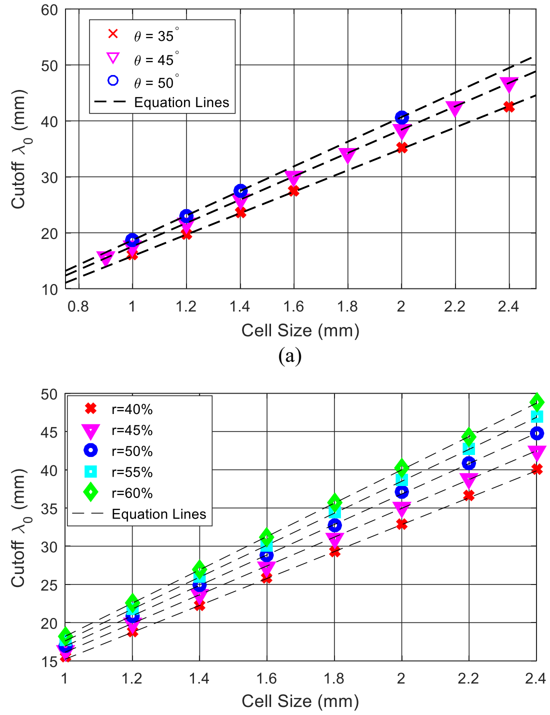

(a)

(b)

Fig. 7. High cutoff frequency matches the predicting equation for: (a) varying angle with a water ratio of 55%, and (b) varying ratio with a flare angle of 45°.

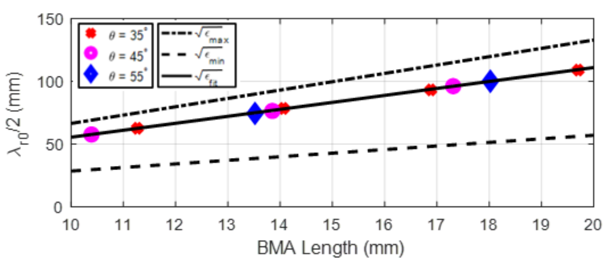

Fig. 8. BMA resonant half-wavelength depends on edge length scaled by the square root of the effective permittivity.

of the factors that increase impedance, θ and r. This is because the effective permittivity of the unit cell increases dramatically as the cell becomes electrically large, as shown by the dashed blue lines in Fig. 6(b).

$$\lambda_0 = aK - 0.006r \text{ (1a)}$$

$$K = 21.811 - 15.172\ \ln(\cos\theta) + 8.317\ln(r) - 5.785\ln(r)\ln(\cos\theta) \text{ (1b)}$$

Verification of these equations is shown in Fig. 7 that plots the free space cutoff wavelength (λ_0) against the cell size (a) for varying flare angle (Fig. 7(a)) and varying fill fraction (Fig. 7(b)). The predicting Eq. (1) is super-imposed in dashed lines, showing excellent agreement (error smaller than 1.75% in all cases). The slope, K, is around ~20 for these plots, which coincides with our results from the PWEM. The inverse of this K value is 0.05, which is a typical first band limit for a rectangular unit cell. Indeed, Fig. 6(a) shows that around 0.05a, the shape of the band begins to no longer be truly elliptical in the z-direction, thus indicating that the effective medium limit is being reached.

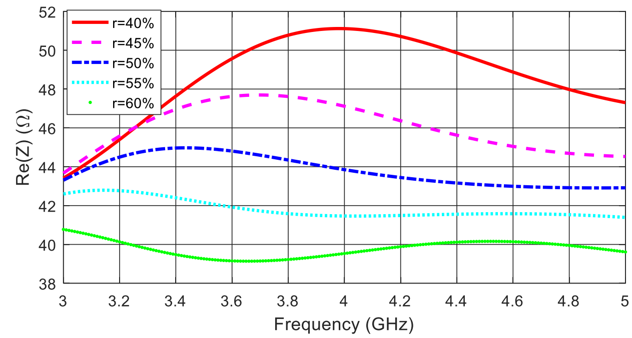

Fig. 9. Increasing water ratio (r) decreases the real input impedance.

B. *Low Frequency Cutoff*

The BMA can be modeled as a quasi-conical antenna with a loaded dielectric that focuses radiation. Similar to a conical antenna, the first resonance in the BMA occurs when its edge length (L in Fig. 1(b)) is equal to an electrical half-wavelength. This is modeled by Eq. 2 that relates the resonant free-space wavelength (λ_{r0}) to the BMA edge length (L) and the effective permittivity (ε_{eff}).

$$\frac{\lambda_{r0}}{2} = L\sqrt{\varepsilon_{eff}} \text{ (2)}$$

The flux developed, which depends on ε_{eff}, is not solely influenced by the maximum permittivity direction. Instead, since the electric fields are normal to the flares, there will be a component of the flux developed that is in the lower permittivity direction. This lowers the wave impedance as compared to if the wave solely propagated in the high permittivity direction. To study this, numerous BMAs with rectangular unit cells (r=55%) of varying height and angle were simulated against skin. The resonant half-wavelengths are plotted against BMA edge lengths in Fig. 8, as well as the maximum $\sqrt{\varepsilon_r}$ and minimum $\sqrt{\varepsilon_r}$ calculated from the PWEM. As shown, the curve of best fit for the permittivity lies between the maximum and minimum permittivity lines. The ratio of the fit, which directly relates to wave impedance, in this instance is 83.5% maximum permittivity and 17.5% minimum permittivity. This ratio of the fit will change based upon the water's dispersion over the bandwidth. Moreover, the dispersion of water would also manifest as nonlinear permittivity slopes between the resonant half-wavelengths and the edge lengths if plotted over a significantly large bandwidth.

C. *BMA Input Impedance*

The BMA's real input impedance can be explored as a function of its: (a) water content and (b) flare angle. To test this, a rectangular unit cell BMA of height 10 mm and flare angle 45° was simulated against a homogeneous skin block. Since the water has a high permittivity, it also has a low impedance. Therefore, increasing the water content (r) of the BMA is anticipated to decrease its real impedance as shown in Fig. 9.

This is the author's version of an article that has been published in this journal. Changes were made to this version by the publisher prior to publication.
The final version of record is available at http://dx.doi.org/10.1109/TAP.2019.2948727

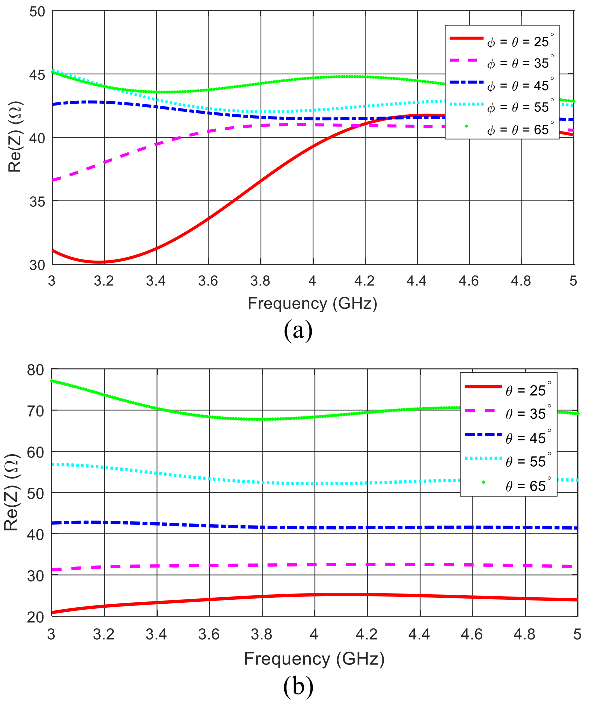

Fig. 10. Real impedance increases: (a) with increasing flare angles θ and ϕ, and (b) dramatically with flare angle ϕ varying and θ=45°.

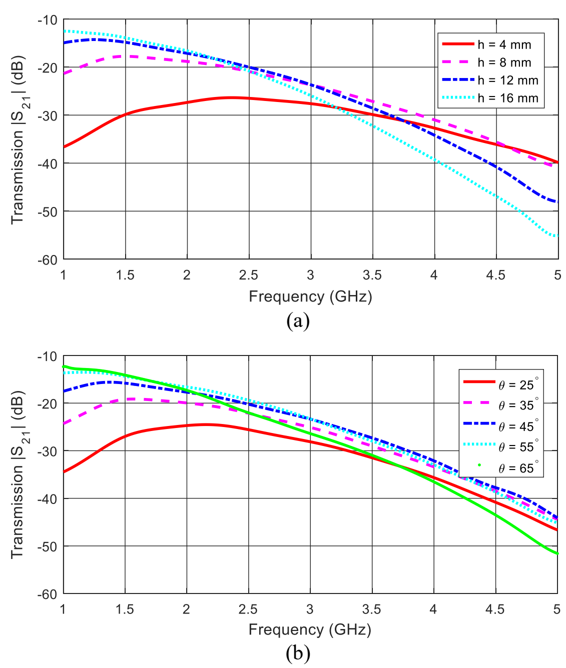

Fig. 11. Transmission loss between identical BMAs vs. frequency plots for: (a) varying height, and (b) varying flare angle of the BMA.

Moreover, the flare angle of the BMA can be modified in order to further control its impedance. Similar to a conical antenna, narrower flare angles are expected to lower the input impedance and wider flare angles are expected to raise the input impedance as shown in Fig. 10(a). If the θ angle (normal to the flare) is different from the ϕ angle (parallel to the flares), this effect will be more pronounced as shown in Fig. 10(b). In this case, ϕ =45° and θ varies.

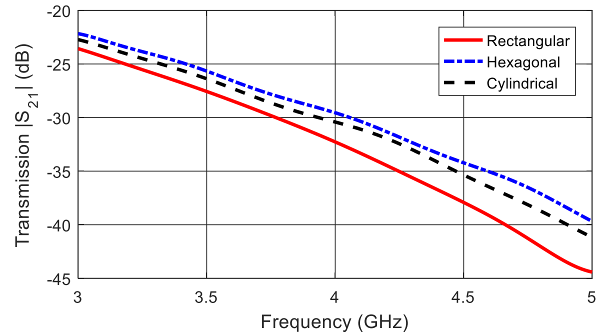

Fig. 12. Transmission between identically sized BMAs through 3 cm for varying frequency.

D. *Transmission Loss*

The BMA gain is dependent primarily on its size, quantified by the flare contact angle, θ, and height, h. The general trend is that a BMA's transmission loss is smallest towards its lower operating frequency. This is expected, because larger BMAs have higher material loss. Also, larger BMAs develop a wider beam, which will have increased loss with frequency as well. To demonstrate these effects, two rectangular unit cell BMAs (h=10 mm, r=0.55) were simulated on both sides of a 30 mm block that had the electrical properties of skin. Transmission vs. frequency plots indicate that larger BMAs have sharper transmission degradation with respect to frequency than smaller ones, as shown in Fig. 11. This indicates that a BMA should be designed for minimum necessary size, so that it has minimal transmission loss across its bandwidth. At frequencies lower than the low frequency cutoff, the antenna will have lower transmission than higher frequency, in-band transmission.

E. *Applicability to Other Unit Cells*

Simulations and theoretical modeling for hexagonal and cylindrical cells indicate that Eq. 1(a) is robust and accounts for a wide variety of designs. Expectedly, the slope, K, will vary depending on the type of unit cell included. Different unit cells have different effective medium limits and would therefore have different slopes.

Section IV.B depended primarily upon the permittivity developed by the unit cell. As such, using the PWEM to analyze the permittivity will allow for the direct use of Eq. 2. Further, the real input impedance can still be manipulated as mentioned in Section IV.C regardless of the type of unit cell.

To discern the effect of unit cell type upon transmission loss, the setup of Fig. 11 was employed again and the BMA cells were altered between rectangular, hexagonal and cylindrical. In all three cases, the unit cell size and water ratio were maintained roughly the same. Transmission loss for varying frequency of the BMA is plotted in Fig. 12. As seen, hexagonal unit cells have the least amount of loss. This was expected since hexagonal unit cells are the most anisotropic [23] per discussions in Section III.C.

(a) (b)

Fig. 13. Experimental set-ups employed in this study: (a) POPEYE leg phantom, and (b) 80% lean ground beef phantom.

V. Measurement Verifications

A. BMA Design and Manufacturing

Leveraging our theoretical modeling and design guidelines, in this Section we pose to design a novel BMA of comparable size to [17] but with improved bandwidth and transmission loss. Section IV.A indicated that the high frequency cutoff could be improved through implementing smaller unit cells, whereas Section IV.B showed that increasing the size of the antenna can lower the first resonant frequency of the antenna, thus lowering the low cutoff frequency. Lastly, Fig. 12's analysis of unit cells showed that hexagonal unit cells are optimal for transmission. Implementing these improvements results in an improved antenna over [17] with only a minor increase in antenna size.

With the above in mind, a BMA is designed that employs the hexagonal unit cell of Fig. 5(b). The BMA has a unit cell size of 2.476 mm with a hexagon diameter of 1.3 mm. Its height is 11.95 mm and it has an angle of 45°, yielding a final base of size 24.9 x 24.9 mm^2. For comparison, the antenna reported in [17] employed the cylindrical unit cell of Fig. 5(a) of size 3.636 mm. The BMA had a height of 10 mm with an angle of 45°, yielding a final base size of 22 x 22 mm^2.

B. BMA Prototype and Measurement Setup

For fabrication, we 3D printed the BMA design of Section V.A using stereolithography. This was accomplished using the Formlabs Form 2 printer and the rigid resin [33]. The rigid resin was chosen for its high precision and stiffness for small sizes. Its relative permittivity and loss tangent were found to be in the range of ~3-4 and ~0.01, respectively. To simplify our design, we assumed it had comparable characteristics to polylactic acid (PLA) (ε_r = 3.549, tanδ = 0.001 [34]). Once printed, the hexagonal holes were filled with water and the sides were covered with copper tape as shown in Fig. 1(a).

Both SPEAG's POPEYE leg phantom (Zurich Switzerland [35], Fig. 13(a)) and 80% lean ground beef (Fig. 13(b)) were used as phantoms to test the BMA. Both are commonly used as phantom materials to emulate the average human body properties. Their electrical properties are reported in our previous work [17].

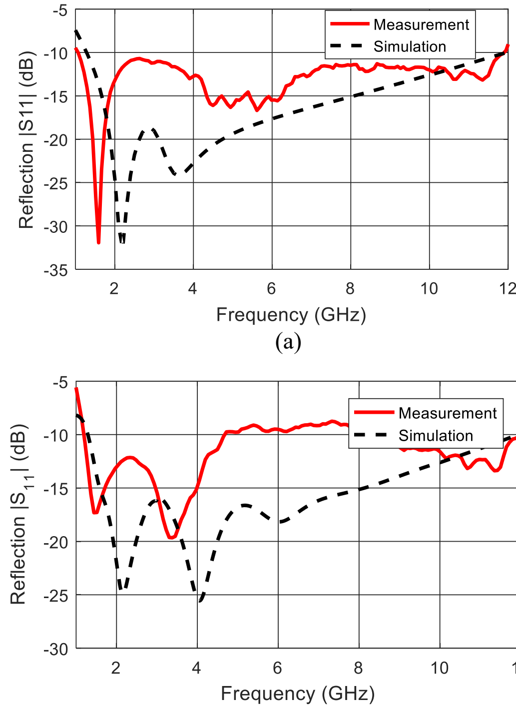

(b)

Fig. 14. Measured and simulated reflection coefficient against: (a) POPEYE phantom, and (b) beef phantom show good agreement.

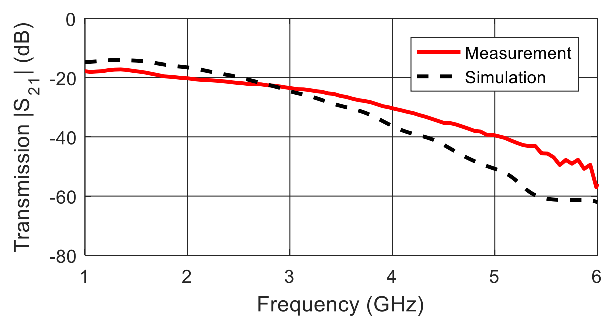

Fig. 15. Measured and simulated transmission coefficients between identical BMAs through beef show good agreement.

C. Results

Measurements and simulations of the BMA's reflection coefficient against the POPEYE and ground beef phantoms are superimposed in Fig. 14(a) and Fig. 14(b), respectively. The measured bandwidth against the POPEYE phantom is 11.12:1, whereas the original design of [17] was merely 6.07:1.

To measure the transmission loss, the ground beef phantom was made to be 3 cm thick and two identical BMAs were placed on either side of it. Referring to Fig. 15, the transmission coefficient was measured and found to be in good agreement with the simulated values. Most likely, there was slight water leakage which caused there to be worse performance than simulation at lower frequencies and better performance at higher frequencies. Beyond 6 GHz, the measurements are in the noise floor and are thus not reported in this paper. At 2.4 GHz, the transmission loss is a remarkable 21.4 dB, which is 6.2 dB lower than [17].

VI. Conclusion

In this paper, we presented BMAs as a new class of wearable, into-body radiators that employ periodic unit cells made of plastic and water to exceed state-of-the-art bandwidth and transmission performance. The PWEM was employed to derive the effective Bio-Matched dielectric properties, and design equations were derived for the high and low frequency cutoffs in terms of the BMA geometry. Effects of varying unit cells (cylindrical, rectangular, and hexagonal) were also discussed. Assuming homogeneous tissue media, we were able to show the general trends of BMA design which can eventually be fine-tuned for various anatomical locations in future. Building on this theoretical framework, a novel BMA was designed, fabricated, and tested with nearly twice the bandwidth and 6.2 dB less transmission loss across 3 cm of phantom material than the most wideband and most efficient into-body radiator previously reported.

The remarkably wide bandwidth and high gain demonstrated in this paper offer new opportunities for medical radiometry and telemetry. This could allow for high resolution in medical thermal imaging, high data rates in implant communication, advancement of multi-channel in-body medical device networks, and other advancements in the exciting intersection of electromagnetics and medicine.

References

[1] D. Rodrigues, P. Maccarini, S. Salahi, T. R. Oliveira, P. J. S. Pereira, P. Limao-Vieira, B. W. Snow, D. Reudink and P. R. Stauffer, "Design and Optimization of an Ultra Wideband and Compact Microwave Antenna for Radiometric Monitoring of Brain Temperature," IEEE Transactions on Biomedical Engineering, vol. 61 no. 7, pp. 2154-2160, July 2014.

[2] N. Livanos, S. Hammal, C. D. Nikolopoulos et al., "Design and Interdisciplinary Simulations of a Hand-Held Device for Internal-Body Temperature Sensing Using Microwave Radiometry," IEEE Sensors Journal, vol. 18, no. 6, pp. 2421-2433 Mar. 2018.

[3] P. Momenroodaki, W. Haines, M. Fromandi and Z. Popovic., "Noninvasive Internal Body Temperature Tracking With Near-Field Microwave Radiometry," IEEE Transactions on Microwave Theory and Techniques," vol. 66, no. 5, pp. 2535-2545, May 2018.

[4] T. Sugiura, H. Hirata, J. W. Hand, J. M. J. Van Leeuwen and S. Mizushina., "Five-band microwave radiometer system for noninvasive brain temperature measurement in newborn babies: Phantom experiment and confidence interval," Radio Science, vol. 46, iss. 5, Nov. 2011.

[5] R. J. Vetter, J. C. Williams, J. F. Hetke, E. A. Nunamaker and D. R. Kipke, "Chronic Neural Recording Using Silicon-Substrate Microelectrode Arrays Implanted in Cerebral Cortex," IEEE Transactions on Biomedical Engineering, vol. 51, no. 6, pp. 896-904 Jun. 2004

[6] R. Sanders and M. Lee, "Implantable Pacemakers," Proceedings of the IEEE, Vol. 84, Iss. 3, pp. 480-486, Mar. 1996.

[7] E. Ghafar-Zadeh, B. Gholamzadeh, F. Awwad and M. Sawan, "Toward implantable glucometer: Design, modeling and experimental results," Annual International Conference of the IEEE Engineering in Medicine and Biology Society, 3-7 July 2013.

[8] A. Mahnama, A. Nourbakhsh, and G. Ghorbaniasl, "A survey on the applications of implantable micropump systems in drug delivery," Curr. Drug Deliv., vol. 11, pp. 123–131, 2014.

[9] C.W. L. Lee A. Kiourti, J. Chae and J. L. Volakis, "A high-sensitivity fully-passive neurosensing system for wireless brain signal monitoring," IEEE Trans. Microw. Theory Tech.,vol. 63, no. 6, pp. 2060–2068, Jun. 2015.

[10] Y. Liu, Y. Chen, H. Lin, and F. Juwono, "A novel differentially fed compact dual-band implantable antenna for biotelemetry applications," IEEE Antennas and Wireless Propagation Letters, vol. 15, pp. 1791-1794, Mar. 2016.

[11] E. Chow, Y. Ouyang, B. Beier, W. Chappell and P. Irazoqui. "Evaluation of Cardiovascular Stents as Antennas for Implantable Wireless Applications," IEEE Transactions on Microwave Theory and Techniques vol. 57, no. 10, pp. 2523-2532, Oct. 2009.

[12] A. Kiourti, J. R. Costa, C. A. Fernandes, and K. S. Nikita, "A broadband implantable and a dual-band on-body repeater antenna: design and transmission performance," IEEE Trans. Antennas Propag., vol. 62, no. 6, pp. 2899–2908, Jun. 2014.

[13] M. Magill, G. Conway and W. Scanlon, "Tissue-Independent Implantable Antenna for In-Body Communications at 2.36–2.5 GHz," IEEE Transactions on Antenans and Propagation, vol. 65, no. 9, Sep. 2017.

[14] H. Bahrami S. Abdollah Mirbozorgi, R. Ameli, L. A. Rusch and B. Gosselin, "Flexible, Polarization-Diverse UWB Antennas for Implantable Neural Recording Systems," IEEE Transactions on Biomedical Circuits and Systems, vol. 10, no. 1, pp. 38-48, Feb. 2016.

[15] L. J. Xu, Z. Duan, Y.-M. Tang, and M. Zhang, "A dual-band on-body repeater antenna for body sensor network," IEEE Antennas Wireless Propag. Lett., vol. 15, pp. 1649–1652, 2016.

[16] J. Felicio, J. Costa and C. Fernandes, "Dual-Band Skin-Adhesive Repeater Antenna for Continuous Body Signals Monitoring," IEEE Journal of Electromagnetics, RF and Microwaves in Medicine and Biology, vol. 2, no. 1, pp. 25-32, March 2018.

[17] J. Blauert and A. Kiourti, "Bio-Matched Horn: A Novel 1-9 GHz On-Body Antenna for Low-Loss Biomedical Telemetry with Implants," IEEE Transactions on Antennas and Propagation, Early Access, 2018.

[18] A. Amar, A. Kouki, and H. Cao, "Power approaches for implantable medical devices," Sensors, vol. 15, no. 11, pp. 28889–28914, 2015.

[19] A. S. Y. Poon, S. O'Driscoll, and T. H. Meng, "Optimal Frequency for wireless power transmission into dispersive tissue," IEEE Transactions on Antennas and Propagation, vol. 58, iss. 5, pp. 1739-1750, Mar. 2010.

[20] S. Kim, J. S. Ho and A. S. Y. Poon, "Midfield wireless powering of subwavelength Autonomous devices," Physical Review Letters, 110(20), May 2013.

[21] D. Nikolayev et al., "Optimal radiation of body-implanted capsules," Physical Review Letters, 122(10), Mar. 2019.

[22] D. Nikolayev et al., "Electromagnetic radiation efficiency of body-implanted devices," Physical Review Applied, 9(2), Feb. 2018.

[23] D. Nikolayev et al., "Robust Ultraminiature Capsule Antenna for Ingestible and Implantable Applications," IEEE Transactions on Antennas and Propagaion, vol. 65, no. 11, pp. 6107-6119, Nov. 2017.

[24] C. A. Balanis, Chapter 13, Horn Antennas, *Antenna theory: Analysis and Design*, 4th Edition, John Wiley & Sons, Inc. 2016.

[25] C. E. Smith, C. M. Butler and K. R. Allee, "Characteristics of a Wire Biconical Antenna," *Microwave J.,* pp. 37-40, Sept. 1979.

[26] C. Gabriel, "Compilation of the dielectric properties of body tissues at RF and microwave frequencies," Report N.AL/OE-TR- 1996-0037, Occupational and environmental health directorate, Radiofrequency Radiation Division, Brooks Air Force Base, Texas (USA), June 1996.

[27] T. Onishi and S. Uebayashi, "Biological Tissue-Equivalent Phantoms Usable in Broadband Frequency Range," NTT DoCoMo Technical Journal, vol. 7, no. 4, pp. 61-65, Mar. 2006.

[28] R. C. Rumpf, "Nonlinear and anisotropic materials," Lecture 3, 21st Centrury Electromagnetics Webseries, CEM Lectures, YouTube, Feb. 2014.

[29] C. R. Garcia, J. Correa, D. Espalin, J. H. Barton, R. C. Rumpf, R. Wicker and V. Gonzalez, "3D Printing of Anisotropic Metamaterials," Progress In Electromagnetics Research Letters, vol. 34, pp. 75–82, 2012.

[30] R. C. Rumpf, "Plane Wave Expansion Method," Lecture 18, Computational Electromagnetics Webseries, CEM Lectures, YouTube, Oct. 2013.

[31] U. Kaatze, "Complex Permittivitiy of Water as a Function of Frequency and Temperature," J. Chem. Eng. Data, vol. 34, pp. 371-374, 1989.

[32] S. Asif, B. Braaten, A. Iftikhar, "Effectiveness of a dielectric probe calibration using deionized, distilled and tap water," IEEE Internaional Syposium on Antennas and Propagation & USNC/URSI National Radio Science Meeting, 9-14 July 2017.

[33] Formlabs, www.formlabs.com, 2019.

[34] E. Huber, M. Mirzaee, J. Bjorgaard, M. Hoyackm S. Noghanian and I. Chang "Dielectric property measurement of PLA," 2016 IEEE

International Conference on Electro Information Technology, Grand Forks, ND, USA, 19-21 May 2016..

[35] Schmid & Partner Engineering AG, www.speag.com, 2019.

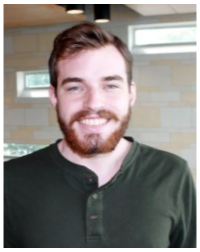

John Blauert (S'14) graduated Summa Cum Laude with B.S. degree in electrical engineering from Rose-Hulman Institute of the Technology in Terre Haute, IN, in 2017.

He is currently pursuing his Ph.D. in electrical engineering at The Ohio State University ElectroScience Laboratory in Columbus, OH under the supervision of Dr. Asimina Kiourti. From 2015 to 2017, he completed internships with Texas Instruments Kilby Labs, Marathon Petroleum and ArcelorMittal. To date, he has authored 2 journal papers and 3 conference papers. His research interests include biomedical applications of electromagnetics research, implanted medical devices, and electromagnetic metamaterials.

Mr. Blauert has been a member of IEEE HKN since 2014. He is also serving as a Reviewer for both the IEEE Journal of Electromagnetics, RF and Microwaves in Medicine and Biology and IEEE Transactions in Antennas and Propagation. In 2018, he was awarded the IEEE Antennas and Propagation Society Doctoral Research Grant.

Asimina Kiourti (S'10, M'14, SM'19) received the Diploma degree in electrical and computer engineering from the University of Patras, Patras, Greece, in 2008, the M.Sc. degree in technologies for broadband communications from University College London, London, U.K., in 2009, and the Ph.D. degree in electrical and computer engineering from the National Technical University of Athens, Athens, Greece, in 2013.

Dr. Kiourti is currently an Assistant Professor of Electrical and Computer Engineering at The Ohio State University and the ElectroScience Laboratory, Columbus, OH, USA. From 2013 to 2016 she served as a Post-Doctoral Researcher and then a Senior Research Associate at the ElectroScience Laboratory. During her career, she has (co-)authored over 40 journal papers, 80 conference papers, and 7 book chapters. Her research interests include wearable and implantable sensors, antennas and electromagnetics for body area applications, and flexible textile-based electronics.

Dr. Kiourti has received several awards and scholarships, including the URSI Young Scientist Award for 2018, the IEEE Engineering in Medicine and Biology Society (EMB-S) Young Investigator Award for 2014, the IEEE Microwave Theory and Techniques Society (MTT-S) Graduate Fellowship for Medical Applications for 2012, and the IEEE Antennas and Propagation Society (AP-S) Doctoral Research Award for 2011. She is currently serving as an Associate Editor for the IEEE Transactions on Antennas and Propagation and the IEEE Journal of Electromagnetics, RF and Microwaves in Medicine and Biology.